Variations in Building-Resolving Simulations of Tsunami Inundation in a Coastal Urban Area

Nobuki Fukui[1]; Yu Chida[2]; Zhongduo Zhang, S.M.ASCE[3]; Tomohiro Yasuda[4]; Tung-Cheng Ho[5]; Andrew Kennedy, M.ASCE[6]; and Nobuhito Mori, M.ASCE[7]

Abstract: The direct simulation of inundation in developed urban areas presents a much greater challenge than the more common bare earth simulations that use roughness, which are used in many tsunami studies. This study intercompares the performance of four longwave models for tsunami inundation on a detailed topographical model of Kainan, Wakayama, Japan, with laboratory results. All simulations include buildings, which have a large impact on overland flood propagation. Inter-model comparisons yield several apparent characteristics: (1) variations between models were small in areas that are always wet; (2) wetting, drying, and overland propagation increased inter-model variation in the inundation front arrival time, maximum water surface elevation, and overland flow velocities; (3) inundated areas and maximum water surface elevations show lower inter-model variation (V) than inundation front velocity and maximum current velocities. Sources for V appeared to occur from differences in wetting, drying, and detailed code implementation rather than major differences in model physics. Using published tsunami fragility models, V led to significant differences in the predicted damage. Differences were largest for fragilities that used velocity and lower for fragilities that only used maximum inundation depths. Based on these results, inundated areas and water levels from building-resolving simulations might be assigned relatively higher confidence, and all the predicted velocities should be considered to have a greater error and potentially should be considered only when using ensembles. **DOI:** 10.1061/(ASCE)WW.1943-5460.0000690.

Introduction

The inundation of developed urban areas during tsunami attacks, combined with the resulting water levels, velocities, and loads, is one of the most important hazard processes that need to be predicted for coastal planning and design in many regions. Large scale tsunami inundation has been reported by numerous destructive mega earthquakes (e.g., the 2011 Tohoku Earthquake tsunami in Tohoku regions, Japan; and the 2004 Indian Ocean earthquake tsunami in Indonesia and etc.). In the 2011 Tohoku Earthquake tsunami, the inundation was larger than expected and infrastructure destruction occurred over a wide area (Mori et al. 2011). Mori et al. (2013) summarized the 2011 Tohoku Earthquake tsunami damage and differences in local tsunami behaviors, such as inundation heights and run-up heights. To minimize the impact of tsunamis and to reduce the number of casualties, the infrastructure destruction along coastal regions in future events and understanding the tsunami inundation over the built environment or coastal urban cities is very important. The modeling of the tsunami inundation processes is essential to design structures, make evacuation plans, city planning, and other activities.

Previously, studies for tsunami inundation tended to use bare earth models, that is, topographies with all structures removed, on grids with a typical resolution of O (100 m) that were much coarser than most building dimensions (e.g., ASCE 2016). The effects of structures are usually included indirectly, typically with increased frictional coefficients in built-up areas. These are thought to give reasonable results; however, there is uncertainty about their detailed accuracy. The numerical models that directly simulate inundation around buildings must have much finer resolution [O (10 m)] than bare earth models, which are sufficient to resolve the outlines of individual buildings and the flow around them. Boundary conditions that incorporate building walls, and the complex propagation of inundation fronts are all important aspects in the prediction of inundation and can vary between models.

Different numerical models for tsunami simulations produce a range of results for identical inputs, which result in a range of uncertainties. Lynett et al. (2017) examined the sensitivity of tsunami-generated coastal current predictions for an inter-model set of simulations and found that shear and separation driven currents were quite sensitive to model physics and numerics. They concluded that deterministic simulations might be misleading for some aspects of tsunamis, in particular, for velocities, and ensemble-based simulations might provide more realistic probabilities for the actual conditions (see also Lynett 2016).

Relatively few studies have examined detailed inundation flows in urban areas using building-resolving simulations (e.g., Cox et al.

[1]Student, Dept. of Civil and Earth Resources Engineering, Graduate School of Engineering, Kyoto Univ., Kyoto 615-8530, Japan (corresponding author). Email: fukui.nobuki.22s@st.kyoto-u.ac.jp

[2]Senior Researcher, Tsunami and Storm Surge Group, Port and Airport Research Institute, Yokosuka, Kanagawa 239-0826, Japan; Student, Dept. of Civil and Earth Resources Engineering, Graduate School of Engineering, Kyoto Univ., Kyoto 615-8530, Japan.

[3]Student, Dept. of Civil and Environmental Engineering and Earth Sciences, Univ. of Notre Dame, Notre Dame, IN 46556.

[4]Associate Professor, Dept. of Civil, Environmental and Applied Systems Engineering, Kansai Univ., Suita, Osaka 564-8680, Japan. ORCID: https://orcid.org/0000-0002-1443-7989.

[5]JSPS Researcher, Disaster Prevention Research Institute, Kyoto Univ., Uji, Kyoto 611-0011, Japan.

[6]Professor, Dept. of Civil and Environmental Engineering and Earth Sciences, Univ. of Notre Dame, Notre Dame, IN 46556.

[7]Professor, Disaster Prevention Research Institute, Kyoto Univ., Uji, Kyoto 611-0011, Japan; Honorary Professor, Swansea Univ., Bay Campus, Fabian Way, Crymlyn Burrows, Swansea SA1 8EN, UK.

Note. This manuscript was submitted on May 22, 2021; approved on August 28, 2021; published online on November 9, 2021. Discussion period open until April 9, 2022; separate discussions must be submitted for individual papers. This paper is part of the ***Journal of Waterway, Port, Coastal, and Ocean Engineering***, © ASCE, ISSN 0733-950X.

2008; Park et al. 2013; Prasetyo et al. 2019). Park et al. (2013) examined flows through an idealized version of Seaside, Oregon that used a Boussinesq model that directly resolved building footprints. Good agreement was found with a set of 1:50 laboratory experiments, once the friction factor was tuned. Surface elevations (η) were moderately sensitive to friction, and velocities and momentum fluxes were highly sensitive. In contrast, Prasetyo et al. (2019) did not examine velocities; however, they reported arrival times and maximum water surface elevations for a 1:250 scale model of an urban area. A two-dimensional (2D) shallow water model tended to underestimate the maximum surface elevations and arrival times, a quasi-three-dimensional (Q3D) model agreed slightly better with the data.

Because of the significantly increased computational cost, Reynolds-averaged Navier-Stokes (RANS) simulations or Large Eddy Simulations of tsunamis through built-up environments are less common. The expense and difficulty of simulating large built-up areas with computational fluid dynamics (CFD) are found in the literature, where a significant number of simulations can be found that examine inundation and loading of one or a small number of structures (e.g., Bagherizadeh et al. 2021; Sogut et al. 2019, 2020; Sarjamee et al. 2017); however, few studied the complex flows around the arrays of many buildings. Pringgana et al. (2021) examined the influence of onshore structures' orientations and arrangements during a tsunami impact that use the numerical method of smoothed particle hydrodynamics, which used the previous experimental results and the resulting hydrodynamic behavior was previously unobtainable in physical experiments. Qin et al. (2018a, b) examined inundation flows using the OpenFOAM model in the same Seaside, Oregon set up as Park et al. (2013). The key findings were that the flows and water levels could be reasonably predicted by the CFD model and with better accuracy than a shallow water 2D model; however, at a significantly increased computational cost. The computational expense was large enough; therefore, the relatively small town was modeled in sections, and it was suggested that "modeling of an entire town could be computationally impractical." Even with significant increases in the available computational power, straightforward simulation of tsunami-like inundation over large built-up areas will not be computationally feasible in the near future. Therefore, groups of shallow water simulations will probably continue to be the primary computational tool to examine inundation in complex regions. However, even for nominally similar shallow water models, nontrivial differences exist in simulations that arise from differences in the model implementation, in particular, for inundation wetting and drying. This provides an additional source of uncertainty in the interpretation of the results, and therefore, it is important to understand the variance in these simulations, and how this relates to the interpretation of the model predictions.

However, the validation of local tsunami inundation behavior in the field is difficult, and observational data are very limited due to the rarity of extreme tsunami occurrence. In addition, it is difficult to measure detailed local phenomena of inundation processes using a physical model due to the complexity of the bathymetry, topography, and interactions between the tsunami flow and macro roughness elements, such as buildings, streets, and topographical changes. These complexities induce turbulence, wave breaking, diffraction, and other hydrodynamic effects. In addition, measurements of surface elevations and velocities on land are difficult due to the limitations of the wave flume and in situ instruments.

This study aims to discuss local tsunami behavior, tsunami inundation, and other hydrodynamic processes on complex land structures in coastal urban areas. First, physical modeling of tsunami inundation in a coastal city is conducted with advanced visualization techniques. Second, a comparison between physical and numerical model results is performed using four different numerical models based on implementations of the nonlinear shallow water equations (2D-SWE). Finally, the sensitivity of tsunami inundation modeling for surface elevations, velocities, and other tsunami characteristics in an urban area is summarized by comparison with physical modeling and numerical results.

Laboratory Experiments

Experiments were conducted at the Hybrid Tsunami Open Flume in Ujigawa laboratory, DPRI, Kyoto University (HyTOFU). The flume is 45 m long and 4 m wide and is can generate tsunami-like long waves or irregular short waves using a combination of a water pump, piston-type mechanical wavemakers, and a dam break gate system (Hiraishi et al. 2015). The 70-kW pump can create a change in water level over time that is similar to a tsunami or storm surge waveform by discharging flow from two 2×0.2 m sized outlets at the flume bed. The maximum pumping capacity is 0.83 m^3/s with a maximum operating time of 1,200 s. The piston-type mechanical wavemaker has a 2.5 m maximum stroke and $\leq$2.83 m/s maximum speed. The wavemaker can generate multiple wave types that include solitary waves and regular or irregular waves $\leq$2 Hz (Tomiczek et al. 2016).

All experiments employed a wooden city model that was based on the city center of Kainan, Wakayama, Japan, which is an industrial city prone to damage from typhoon storm surges and predicted Nankai Trough tsunamis (Mizobata et al. 2014; Le et al. 2019). The 3D city model, which included ports, buildings, and houses, was constructed at 1:250 scale and covered an area of 2 km from east to west and 1 km from north to south (Yasuda et al. 2016). Plan and elevation views of the physical model of Kainan, Wakayama, Japan, are shown in Fig. 1(a). The east (inland) side of the model mainly consisted of residential areas and mountains with an overall higher elevation compared with the coast (west) side. An elevated railway line runs through the city from north to south with a station on the north side of the model. Water could flow through the railway line under the bridge but not through the station, which was a solid structure. The west (coastal) side of the model mainly consisted of the harbor area, with retail stores and warehouses on the north, oil refineries on the south, and a section of steelworks on the northwest. The only entrance to the port from the deepwater region of the model was located in the southwest. The land section of the physical model had a wooden base that was 5.5 cm thick and was placed on a steel plate 0.8065 m above the bottom of the wave flume, and the bottom of the water region was the steel plate. A 1:10 planar slope that reached the bottom of the flume was connected to the west of the model. The design water depth for the experiment was 0.877 m.

In total, 12 wave gauges (WGs) were set up to cover the flume from offshore to onshore and over the city model to measure wave heights during the experiment. WG1 was set up near the wave maker to provide the initial wave condition for the numerical models. Then, WG 2, 3, 6, and 9 were placed in the water region of the city model, with all others on normally dry land. The locations of the WGs are shown in Fig. 2, with the specific coordinates of each wave gauge listed in Supplemental Table S1. Two acoustic doppler velocimetry (ADVs) devices were set up offshore to measure the velocity of incoming waves. Table S2 gives a summary of the measurement items and instruments used in the experiment. The time series of the water surface height of the incident waves used in each case is listed in Table S2 and shown in Fig. S1.

Visualization of the inundation process across the city model for all cases was recorded by an overhead 4K video camera. For

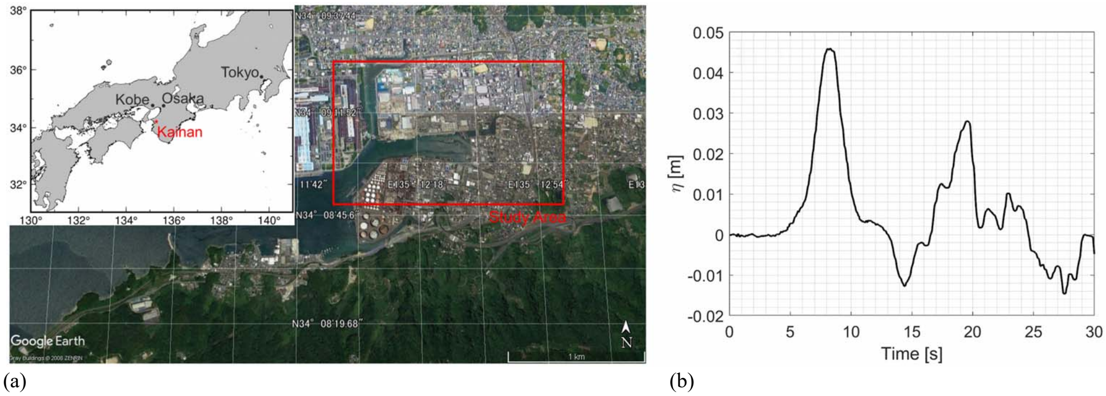

Fig. 1. Summary of the experimental setup: (a) the location of the study area, Kainan, Wakayama, Japan (top left) and overview of the coastal urban area used as a study area; box shows the area for physical experiment and numerical simulations (map data © 2021 Google; Gray Buildings © 2008 ZENRIN); and (b) water surface elevation near the wave generator.

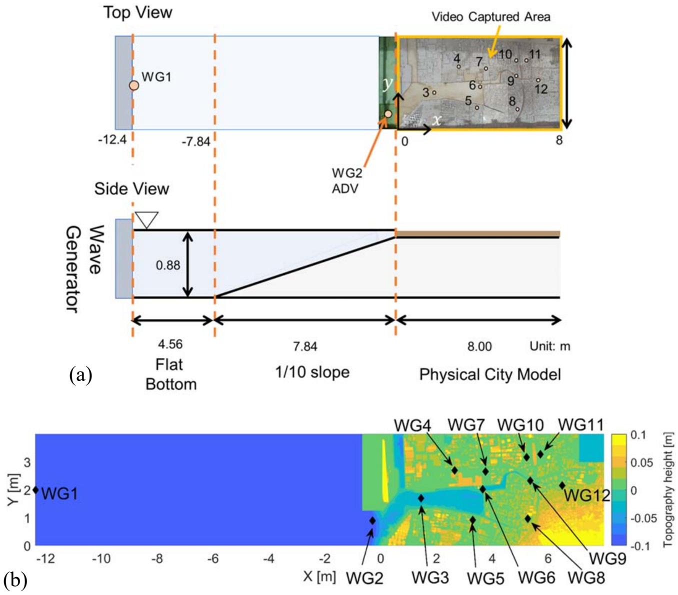

Fig. 2. Experiment flume layout: (a) top and side view of the experiment flume (circle with number shows each WG location) and its dimension (m); and (b) used computational domain (different shades show topography and bathymetry).

selected cases, fluorescent dye (Sinleuchte red dye) was injected into the water area in the city model before the wave forcing; therefore, the leading edge of inundation could be detected in the video images. Particle image velocimetry (PIV) was applied to measure the spatial flow patterns across the city model on several tests that used small 5-mm foam particles that were painted with Sinleuchte fluorescent yellow dye and spread across the model before each experiment. The velocity fields were obtained by super-resolution PIV that used DynamicStudio software (Dantec Dynamics, Skovlunde, Ballerup, Denmark). The measured water velocity over land using PIV is important, because it is difficult to use in situ instruments, such as ADVs in dry or low water level conditions. The estimated flow velocities from the PIV combined with the measured velocities from the ADV were compared with the results from the numerical modeling along with the wave gauge data.

The inundation condition used in this study was a solitary wave 5-cm high at the wave generator, which became 12.5-m high at 1:250 full scale. The assumed time scale of tsunami events was 30 s, which became approximately 475 s at full scale. Solitary wave generation in a tsunami experimental model has been used widely in many previous studies (e.g., Park et al. 2013). However, a solitary wave does not exactly reflect tsunami waves; it is just an idealization of a tsunami wave profile, and those laboratory experiments are not yet applicable to a real-scale tsunami (Prasetyo et al. 2019). The tests in this study were from a much larger series of experiments and included constant flow and realistic tsunami waveforms that will be reported separately.

Numerical Modeling

Numerical Model

In this study, inundation simulations were conducted using four numerical models with different numerical implementations and, to a lesser degree, with different governing equations. The accuracy of the simulation results was compared with the experimental results, and the variability between the models was investigated to estimate the uncertainty in the numerical simulations.

Table 1 gives a list of the governing equations for each model and other conditions about the numerical treatment (e.g., discretization methods for the advection and frictional term, tolerance depth for a frictional term). Brief descriptions and relevant references for each of the models are as follows.

1. TUNAMI-N2 (Goto et al. 1997): TUNAMI-N2 is an SWE model that has been used to simulate tsunami propagation from offshore to inland areas in Japan and other countries. The governing equations of the models are based on the 2D nonlinear SWE in depth-integrated form and are discretized in time with explicit leapfrog finite differences.
2. STOC-ML (Tomita and Kakinuma 2005): STOC-ML is a multilayered model with hydrostatic approximation. The governing equations of STOC-ML are the RANS equations, which are different from the other models in this study. However, the number of vertical layers used in this study was one and the Reynolds stress was ignored in this simulation. Therefore, the governing equations were equivalent to the conventional SWE in velocity form rather than depth-integrated form. Therefore, it differs from the other models used in this study.
3. Subgrid SWE model (Kennedy et al. 2019): The subgrid SWE (SGSWE) model developed by Kennedy et al. (2019) uses the grid-averaged SWE in depth-integrated form as the governing equations, with closure approximations applied to the subgrid

J. Waterway, Port, Coastal, Ocean Eng., 2022, 148(1): 04021044

Table 1. Summary of numerical setup for each model

Item	TUNAMI-N2	STOC-ML	Subgrid SWE	JAGURS
Abbreviation	TUNAMI	STOC	SGSWE	JAGURS
Governing equations	Depth-integrated SWE	Velocity form SWE	Subgrid-averaged SWE	Depth-integrated SWE
Spatial discretization	Finite–difference method			
Spatial differentiation	Staggered C-grid			
Temporal differentiation	Leapfrog scheme		Euler-backward scheme	Leapfrog scheme
Convection terms	Upwind (first-order accuracy)			
Other gradient terms	Centered (second-order accuracy)			
Friction term	Semi-implicit			
Wet/dry boundary	Kotani et al. (1998)		Casulli (2009)	Kotani et al. (1998)
Tolerance depth for wet/dry	10^{-10} m	10^{-6} m	0 m	10^{-6} m
Tolerance depth for convective term	10^{-6} m	No	No	10^{-6} m
Maximum velocity limiter	7 m/s	5 m/s	No	$Fr = 2.0$
Roughness coefficient	Water channel ($X = -12.36$ to -0.66 m): 0.025 Physical model ($X = -0.66$–8.0 m): 0.013			
Input boundary	$X = -12.6$ m along the left boundary (WG1)			
Boundary conditions	North and south: wall boundary West: inflow boundary East: radiation boundary			

system to enhance the accuracy when saving computational resources. The equations are discretized in time with an Euler-backward finite–difference scheme, and in space using a staggered finite–difference grid.

4. JAGURS (Baba et al. 2015): JAGURS solves the linear and nonlinear depth-integrated SWE by implementing a staggered-grid, leapfrog finite–difference scheme. A nested grid system is adopted to enable higher spatial resolutions in the target domains. The code has been parallelized for high-speed computation.

Numerical Setup

Fig. 1(b) shows the measured water surface elevation at WG1 that was used for wave input at the west (ocean) side computational boundary. A free transmission condition was applied at the open boundary on the east side. The boundary conditions for the north and south sides used wall boundaries with slip conditions. For the lateral wall effect, the authors checked the velocity and flow direction near the north and south wall boundaries that were measured by PIV. Some wall effects were limited to within 5 cm along the wall. In addition, the bottom wall effect might exist since the velocity measured by PIV only showed the one at the top layers. The total computational time was 30 s, which allowed inundation by the incident wave to be completed, and did not consider waves re-reflecting from the wavemaker. The movie that was used for a series of image analyses showed that the reflected wave started to inundate the land area after 25 s and contaminated the measured data. The authors used incident wave data that included the wave reflection from the wavemaker and removed the computational results from 25 to 30 s.

Fig. 2(b) shows the topography and bathymetry in the numerical domain. The elevation data for the domain of the physical city model ($X \geq 0.0$ m) were created by interpolating the scanned point cloud data into a regular grid. Point data were obtained with a laser scanner (Leica BLK360 produced by Leica Camera AG, Wetzlar, Germany) set up at three locations in the basin, with the results combined into one data set. For the grid size, the convergence tests that changed the grid size between 1.0 and 0.5 cm was conducted before the main computations, and this confirmed that there were no significant differences in maximum surface elevation and velocity between two different grid size cases. Therefore, 1.0 cm grid resolution was chosen to reduce the computational time, which resulted in a domain of $2{,}037 \times 400$ points. The bottom roughness was based on the Manning model with roughness coefficients of $n = 0.025$ for $X < -0.66$ m and $n = 0.013$ for the domain of the physical city model ($X > -0.66$ m) based on the land use that followed Kotani et al. (1998). Manning's roughness coefficients for the physical model area were smaller than the one for the ocean bottom since the value of 0.010–0.013 for Manning's roughness is recommended for artificial channels that are made by smooth wood (e.g., Chow 1959). Note that the model input (e.g., bathymetry, incident wave, and roughness) was unified and no self-filtering schemes to handle the large gradient of bathymetry due to buildings were implemented for all the numerical models (TUNAMI, STOC, SGSWE, and JAGURS).

Results

This study used two types of data, point gauge and spatial data, and compared the model results against each other and with the laboratory results. The magnitude and time of maximum surface elevation at selected locations were examined for point data. In addition to the arrival time, wavefront velocity, fluid velocity, and surface elevation (maximum value and temporal change) were examined in the spatial data by visualization analysis of the laboratory experiments and compared with the numerical results.

Model Variation and Accuracy of Point Gauge Data

Fig. 3 shows η at WGs 2–3 that were installed at the entrance and center of the port [locations in Fig. 2(b)] for confirmation of the incident wave condition. All models showed good agreement with the experimental data at WG2. However, for all models, the maximum surface elevation was approximately 0.01 m (15%–20%) smaller than the measurement at WG3, although the absolute magnitude was small. This might either have been caused by attenuation near the entrance of the port by sea bottom friction that was larger than the experiment, more probably from dispersive effects that were not included in these hydrostatic models, or wall effects in the experiment. Since the results on land tend to be underestimated due to the influence of these biases of incident waves, this should be considered. Fig. 4 shows the relationship between the modeled maximum surface elevations and their peak times. The

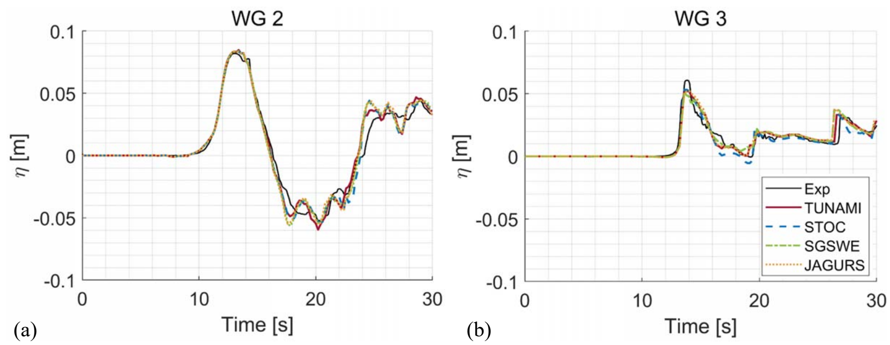

Fig. 3. Time series of water surface elevation at (a) bay mouth (WG2); and (b) center of the port (WG3); different lines show models or experiment (solid line = experiment; bold line = TUNAMI; dashed line = STOC; dashed-dotted line = SGSWE; and dotted line = JAGURS).

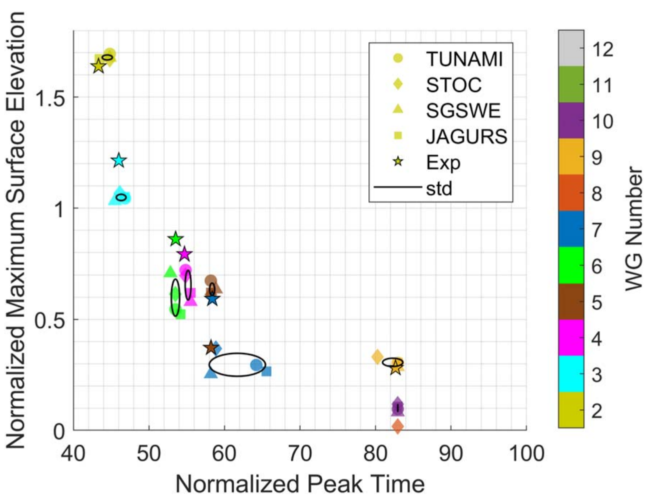

Fig. 4. Maximum surface elevation at each WG and its appearance time (peak time) normalized by the incident wave in Case H05; Marker (circle = TUNAMI; diamond = STOC; triangle = SGSWE; square = JAGURS; and star = experiment) different shades WG number and ellipsoid shows standard deviation.

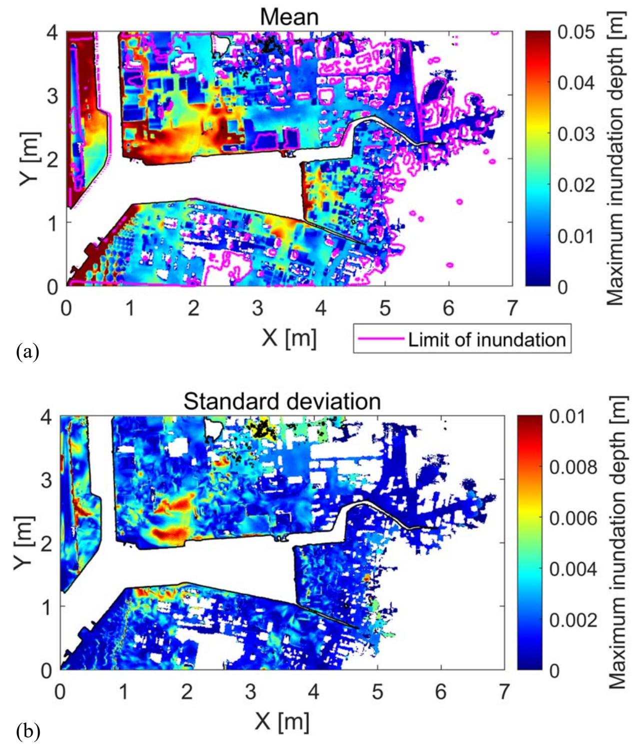

Fig. 5. Showing (a) μ; and (b) σ of maximum inundation depth (light solid line shows the maximum inundation leading edge observed in the experiment).

η and times were normalized by incident wave conditions as

$$\bar{\eta} = \eta/\eta_0 \tag{1}$$

$$\bar{T} = T/T_0 \tag{2}$$

where $\eta_0 = 5.0$ cm (wave height at WG1); $T_0 = \sqrt{h/g}$; and $h = 0.877$ m (depth of the wave flume); and $g = 9.81$ m/s^2, respectively. All the models showed similar tendencies where they tended to underestimate the maximum surface elevation. The ellipsoids in Fig. 4 show the mean (center of ellipsoids) and standard deviation (radii) of maximum water surface elevation and time of peak water levels for the four model results at each gauge location. The larger deviations were observed at locations further inland (WGs 4, 5, and 7) and in very shallow inundation depths (WG 6 and 9) and the differences were smaller in deeper water (WGs 2 and 3). Focusing on gauges in the inundated regions, WG4 (road in the flat area), and WG 7 (intersection of buildings) gave approximately a 4.7 and 3.7 times larger standard deviation in η than WG3 (in the port). In addition, the arrival times of the peak inundation had a large standard deviation (approximately 5.8 times larger than WG3). WG4 and 7 were installed on a wide road but large buildings on both sides of the road complicated the simulations. Furthermore, WG7 was at a location where two major inundation wavefronts merged from the west and the south. The complexity of inundation appeared to be a major reason why the model variations here were larger than in deep inundation areas. More detailed inundation processes around the intersection are presented in the following section.

Model Variation and Accuracy of Spatial Data

Numerical results about the spatial (or spatiotemporal) data are discussed to examine the inter-model variation (V). To estimate model uncertainty for any computed property, the relative magnitude of V in each value is defined as

$$V = \sigma/\mu \tag{3}$$

where V = variation; σ = model standard deviation; and μ = model mean value.

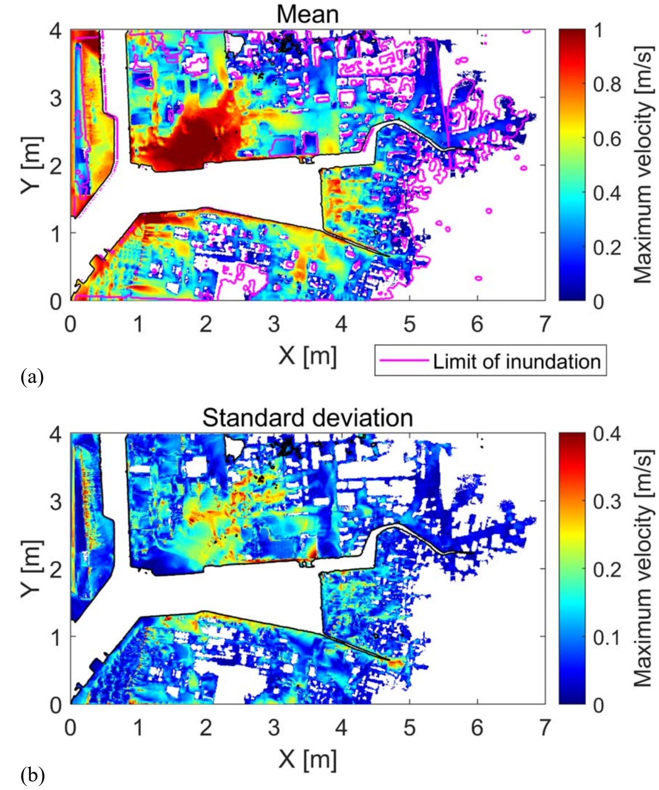

Fig. 6. Showing (a) μ; and (b) σ of maximum velocity (light solid line shows the maximum inundation leading edge observed in the experiment).

Maximum inundation depth and overall limits of flooded areas are two important measures for tsunami intensity and are widely used for tsunami hazard maps. Fig. 5 shows μ and σ of the maximum inundation depth in each grid. The inundation limit of the tsunami leading edge from the experimental data is shown in Fig. 5(a). The overall inundated area from the model results agreed well with the experimental data, and therefore, the inundation limits could be reproduced by the numerical models. Focusing on the maximum inundation depth, the mean value of the inundation tended to be larger at areas close to the original shoreline. For instance, deeper inundation depths of >0.03 m (7 m at full scale) were recorded in the north nearshore area ($X=1$–2 and $Y=2$–2.5 m). The inundation depth in the middle nearshore area ($X=3.8$–4 and $Y=1$–2 m) was recorded as >0.05 m (12.5 m at full scale) depth. The V in the inundation depths in the models changed significantly depending on areas but demonstrated some general patterns. Large areas of the model results showed standard deviations <0.004 m (1 m at full scale), but some areas had larger variance. Specifically, the nearshore north ($X=1$–2 and $Y=2$–2.5 m) and south ($X=1$–2 and $Y=1$–1.2 m) areas show large deviations (>0.006 m; 1.5 m in real scale) of maximum inundation depth. These were near the locations of the first inundation, and the large variation appeared to be related to the dynamic wetting, drying, and propagation of the large-amplitude wavefront. In these areas, $V=0.17$ and 0.24 on average in the nearshore north and south, respectively.

Fig. 6 shows μ and σ of the maximum fluid velocity in the same format as shown in Fig. 5. The mean value of the velocity tended to be larger in areas close to the original shoreline, similar to the inundation depth. Furthermore, the velocity was locally amplified even at the areas where the jet-type channelized flow was caused by the road or the small alley between buildings. For example, in the middle nearshore area ($X=3.8$–4 and $Y=1$–2 m), the mean value of velocity was 0.5 m/s (7.9 m/s at full scale), but >0.8 m/s (12.6 m/s at full scale) was observed between the buildings. The large standard deviation of the velocity was given in the road or small alley between the buildings and approximately >0.3 m/s (4.74 m/s at full scale) was recorded in the middle nearshore area ($X=3.8$–4 and $Y=1$–2 m). In addition, the nearshore north ($X=1$–2 and $Y=2$–2.5 m) and south ($X=1$–2 and $Y=1$–1.2 m) areas showed large deviations similar to the inundation depths (>0.35 m/s; 5.53 m/s in real scale). The $V=0.54$, 0.17, and 0.33 on average in the nearshore middle, north, and south, respectively.

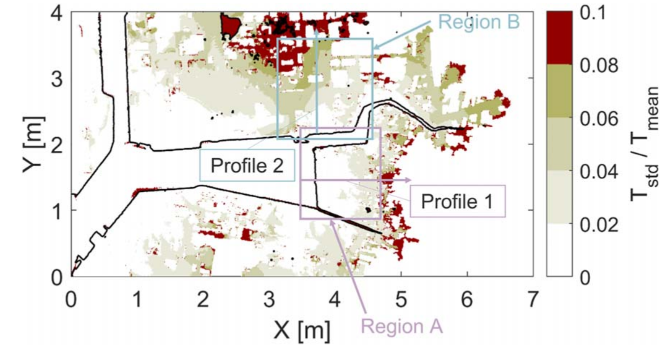

Fig. 7. Spatial distribution of variation (ratio of σ to μ) of arrival time (dark line shows shoreline).

The arrival time of the inundation front is important in tsunami inundation modeling for evacuation planning (e.g., Wang et al. 2016). Inundation front propagation is a complex function of the detailed numerical wetting and drying choices combined with the implementation of convective momentum, surface gradients, building boundaries, and other aspects near the moving wet–dry front. The spatial distribution of inundation arrival time variation is shown in Fig. 7. Arrival time inter-model variations near the harbor and close to shorelines are uniformly small, with large areas showing $V<0.04$. Inland, a larger variation was observed, because the run-up distance was long and inundation depends on the direct distance from the shoreline and potentially complex flow paths. For example, for Region A shown in Fig. 7, the dimensionless variation was $V<0.02$ near the shoreline, and in Region B, the variation was >0.04 at approximately $X=3.5$ and $Y=2.2$ m although the direct distance from the shoreline was short. This appeared to be because inundation here came overland from the west and had already traveled a long distance over land.

To investigate the major factors that cause differences in the model inundation arrival times, wavefront velocities from the models and experiments were compared along a one-dimensional transect. The inundation leading edge was detected at the grid cell where the inundation depth changed from zero to any positive value. The wavefront velocity was calculated as the ratio of the displacement of them to the time required. Fig. 8 shows the laboratory and model inundation front velocities along Profile 1 [Region A (Fig. 7)]. Of note, sea ($X=3.5$–3.7 m) and land ($X=3.7$–4.8 m) were included in this transect. The results showed that the difference in inundation front velocity between the four models was more than twice as large inland compared with the flow in the harbor. This inland speed variation was approximately 20%–30%. The different models had very consistent tendencies: STOC gave the fastest speeds and TUNAMI, JAGURS, and SGSWE followed in order. All the models showed similar tendencies; however, STOC and TUNAMI gave the closest agreement with the experimental results. The inundation front velocity from STOC was closest to the experiment

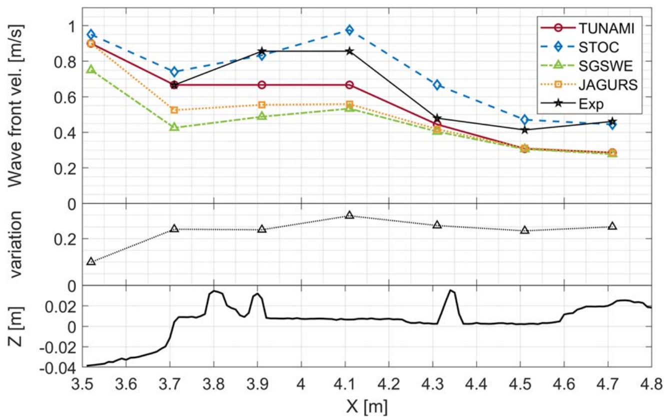

Fig. 8. Wavefront velocities by models (top), their variation estimated the same as in Fig. 7 (middle), and topographical change (bottom) at Profile 1 shown in Fig. 7; dashed lines show numerical results (refer to Fig. 3), and dark solid line shows experimental results.

(within 15% error) in the plain area (e.g., $X = 3.9$–4.1 m) and TUNAMI was the most accurate around buildings ($X = 3.7$–3.9 m). These results showed the blocking effect by buildings was well modeled by TUNAMI and the contraction flow was well modeled by the STOC. However, all models except for STOC underestimated the wavefront velocity behind the first group of buildings ($X = 3.9$–4.3 m) and the error ranges were approximately 10%–40%. The observed variations in the inundation front velocity were mainly caused by the variation in the fluid velocity in the inundated areas which, along with maximum elevation variation, will be discussed in the following paragraph.

Maximum fluid velocities and surface elevations along Profiles 1 and 2 represented another avenue for comparison. Fig. 9 shows a comparison of the model results for maximum surface elevations, and maximum velocities and include the PIV results from the laboratory experiments. For the laboratory data, only high-reliability (high particle density) PIV results were included. In Profile 1 [Fig. 9(a)], all model velocities showed similar trends, with reasonably good agreement with the experiment and between each other. However, as with the inundation front velocities, the magnitudes of maximum current velocities differed. The maximum current velocity estimated from STOC was the largest and TUNAMI, JAGURS, and SGSWE followed in the same decreasing order as the inundation front velocity. The V in the maximum current velocity was more than twice as large as in surface elevation, although the V in the maximum surface elevation was small. Furthermore, the maximum current velocity variation was large around buildings. Specifically, the velocity V was approximately 0.5 at $X = 3.88$ and 4.35 m where large buildings (>7.5 m full scale) were located. However, care should be taken when placing significance to the large variation at $X = 4.63$ m since the velocity was much smaller than other areas. The source of the velocity difference will be examined in the section "Discussion."

The inter-model comparison in Profile 2 is shown in Fig. 9(b). Of note, maximum current velocity and surface elevation were similar in each model, but model velocity magnitudes followed the same trends shown in Profile 1. There are two characteristic areas to be discussed: (1) a road intersection at $X = 2.5$–2.9 m and (2) a building area at $X = 3.0$ m. In particular, the intersection showed different characteristics than other locations. Here, the maximum current velocity variation was approximately 0.18 and larger differences from the experimental results were observed. Note that the variation in maximum current velocity was similar between the intersection ($X = 2.5$–2.9 m) and shoreline ($X = 2.2$ m) but each model gave quite different values at the intersection and all models except for STOC were quite close to each other and the measured values at the shoreline. The variation in maximum surface elevation was smaller than that for maximum current velocity. However, the velocity variation was still larger than Profile 1, although the number of buildings was smaller. One of the reasons was that the flow here came from two directions, and the flow at the intersection from the west blocked the flow from the south. The previous results showed that the maximum current velocity was quite sensitive to the model used. Possible reasons for such variations in this and other properties will be considered in the section "Discussion".

Then, the spatiotemporal uncertainty was examined, which focused on the leading edge of inundation. Fig. 10 shows a time series of inundation leading edges every 0.2 s from the start of the inundation in Region A. Note that the time steps shown on the title represent the elapsed time from the wave arrival at the shoreline. Little difference in inundation leading edge was observed before arrival at the first group of buildings [X (shown in Fig. 10 by the dark-colored box)]. However, the difference gradually increased after passing building X. The STOC and TUNAMI models were closer to the experiment than SGSWE and JAGURS. After passing the second group of buildings [Y (light-colored box in Fig. 10)], the leading edges from STOC and the experiment were furthest and the ones by the other models were underestimated. At the final snapshot (1.0 s), differences between models were maximum and the leading edge of the inundation front varied from 4.2 to 4.4 m. The STOC model showed the fastest inundation, and the laboratory experiments, TUNAMI, JAGURS, and SGSWE followed in decreasing order, which agreed with the previous analyses. The same analysis was performed in Region B and a smaller variation in the inundation leading edge was observed (not shown). Such differences depend on the cross-shore velocity and will be discussed in detail in the following sections.

To investigate the inter-model differences during inundation in detail, the spatiotemporal changes in surface elevation and velocity in the model are shown in Fig. 11. Figs. 11(a–d) shows the snapshots of surface elevation and velocity in Region A when the modeled inundation leading edge arrived at the second group of buildings [Y given by the light-colored box shown in Fig. 10(a)]. These arrival times were different in each model, as shown in this figure, and reflected the differences in the inundation velocities. The results of TUNAMI and STOC showed similar tendencies for surface elevation: the total inundation area with depths >0.01 m was smaller for these models than for SGSWE and JAGURS. The local variations in the surface height along the buildings and channels differed model by model. Fig. 11(e) shows cross sections of the cross-shore velocity and surface elevation at the same time as shown in Figs. 11(a–d) along Profile 1. The cross-shore velocity was divided into the same groups as shown in Figs. 11(a–d). The values near the first group of buildings were closer to each other between the TUNAMI and STOC models, and their difference was within 5%. However, STOC gave approximately a 30% larger cross-shore velocity near the inundation leading edge ($X = 4.0$–4.1 m) than TUNAMI. STOC tended to give a large velocity in small areas that were surrounded by buildings, such as roads. The SGSWE and JAGURS were close to each other in the whole area along Profile 1, and their difference was within 10%. In addition, the cross-shore velocities that were modeled by the SGSWE and JAGURS were smaller than TUNAMI and STOC around the first group of buildings. For surface elevation, patterns for each model were more visible. TUNAMI and STOC showed a gentle slope of surface elevation near the leading edge ($X = 4.0$–4.1 m) and SGSWE and

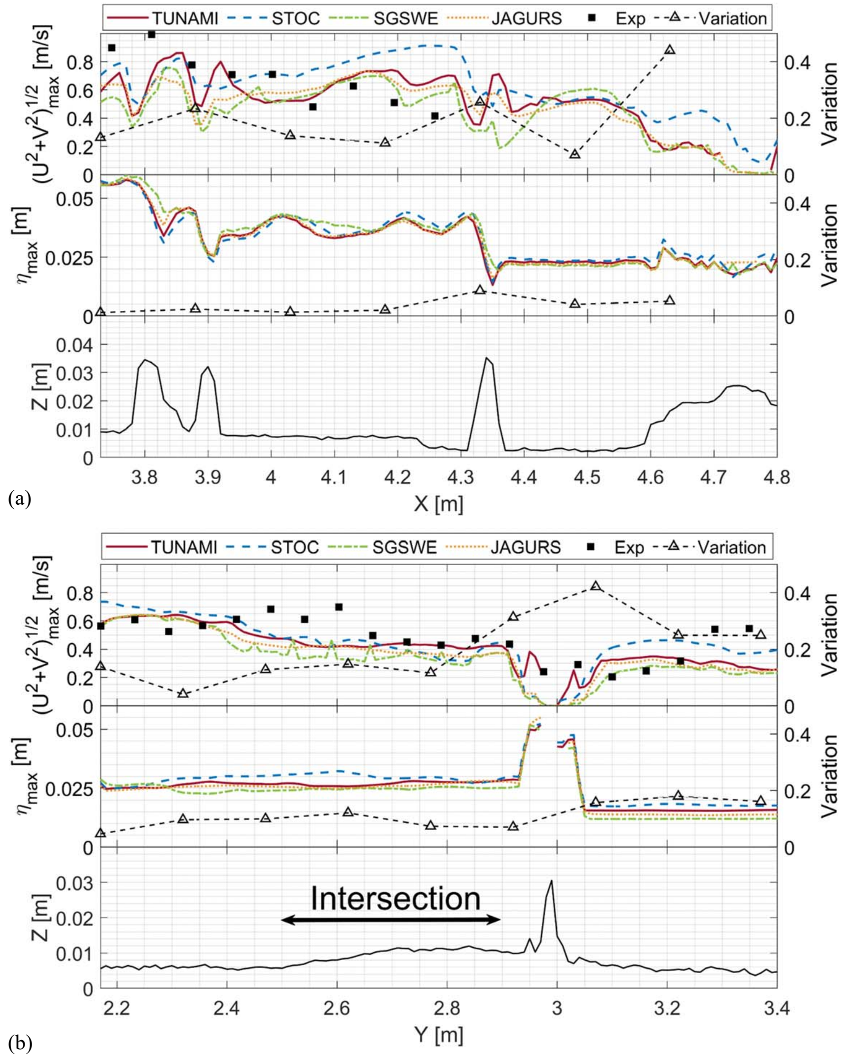

Fig. 9. Maximum velocity magnitude (upper), η (middle), and topographical change (bottom) at Profiles 1 (middle part of the city) and 2 (north part of the city) shown in Fig. 7; solid line (refer Fig. 3) shows numerical results, square shows experimental results, and dashed line shows variation (ratio of σ to μ).

JAGURS showed steeper slopes. There was about a 55% difference in surface elevation between both groups.

Finally, the spatial–temporal uncertainty was examined by focusing on the inundation for the merging flow. Fig. 12 shows the difference in the merging flow at the intersection in Region B. The times were different for each model and were chosen so that in each model the inundation leading edge arrived at the north side of the intersection as the flows merged. Note that surface elevation at velocity when the flows from the south and east merged are shown. There was a noticeable difference in velocity and surface elevation between the models, especially around the intersection (marked with a circle). For example, the TUNAMI and STOC gave approximately 0.023 m surface elevation and the SGSWE and JAGURS gave approximately 0.015 m. In addition, the current velocity and direction differed. TUNAMI and JAGURS showed flow in the north direction but not in STOC. In addition, SGSWE showed north directional flow; however, some velocity directions were different (northwest). The major flow direction was determined by the blocking effect of the flow from the west. A larger current velocity from the west gave a larger blocking effect for the flow from the south and vice versa. The larger blocking effect leads to the local amplification of surface elevation. The series of differences in the inundation process was mainly due to the arrival time of the flow from the west since the variation was ≥1.5 times larger than that from the south. This type of inter-model variations in the arrival time gave the differences in momentum fluxes that were transported from the west and the strength of the blocking effect. The factors for the variation in the detailed inundation process with a series of analyses will be shown in the section "Discussion".

Discussion

This study investigated the reproducibility of tsunami inundation experiments using four different numerical models. All the numerical models could reproduce the inundation process overall; however, the detailed local behavior of hydrodynamic quantities, such as surface elevation at the intersections or velocity around buildings varied between the models. The source of the differences in the numerical models and results is discussed in detail based on the inter-model comparison. Four main factors caused the variation in the numerical results between the four models: (1) differences in advection term and temporal discretization; (2) bottom friction term discretization; (3) wet/dry boundary conditions; and (4) differences in the formulations

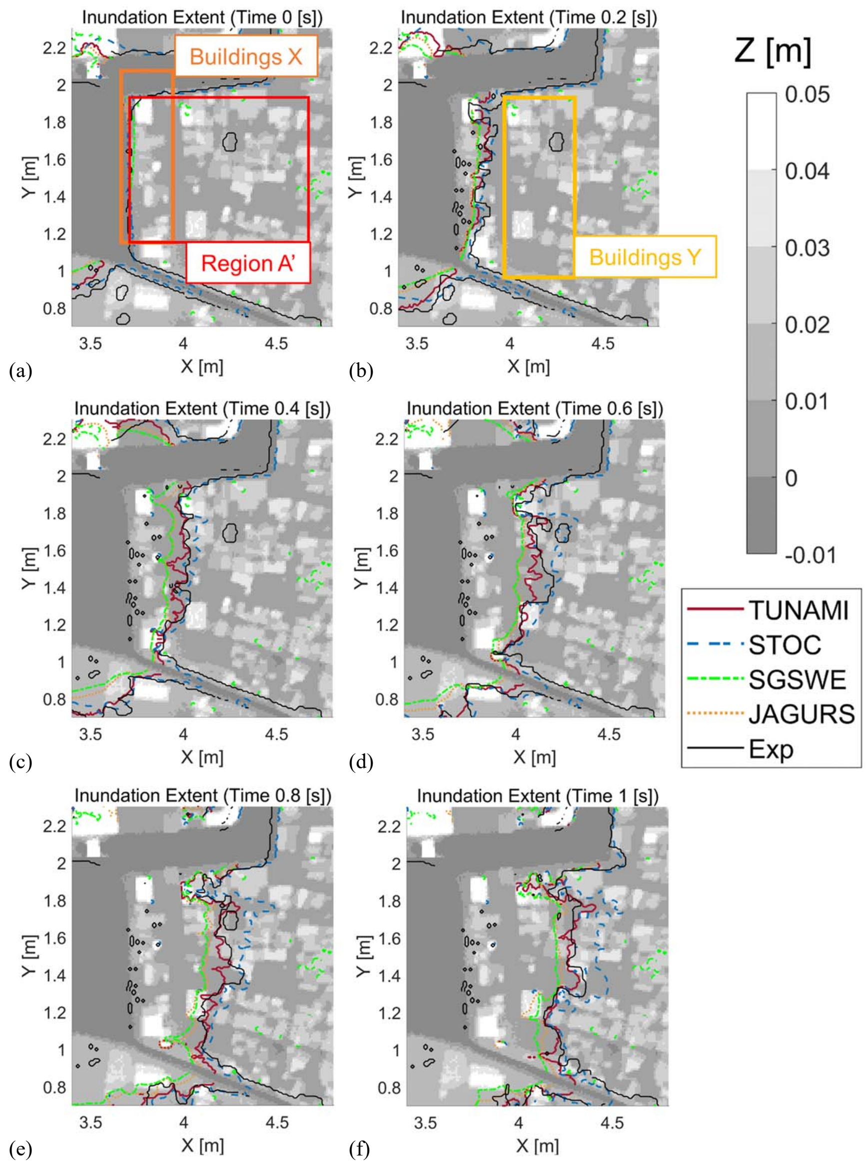

Fig. 10. Inundation leading edge (refer Fig. 3) in time series at Region A shown in Fig. 7 from the starting time of inundation: (a) 0 s; (b) 0.2 s; (c) 0.4 s; (d) 0.6 s; (e) 0.8 s; and (f) 1.0 s after starting inundation. Boxes show groups of buildings X and Y where flow arrived first and second, respectively.

of the governing equations (velocity, depth-integrated form, subgrid, conservative, or nonconservative form). The fundamental discretization schemes for the bottom friction and advection terms were similar between each model but there are differences in the detailed treatments. It remains unclear how such differences affected the variations in the inundation processes; however, this is one of the main reasons for the presented variation in the numerical results.

A small variation in velocity and surface elevation was observed in the offshore area away from the port and only SGSWE showed a slightly slower propagation speed. Here, the effect of the friction term was minor for tsunami propagation offshore since the effect of the advection term was small in the offshore area. The differences here probably resulted from the backward Euler time-stepping in the SGSWE versus the leapfrog scheme in the other models. However, the velocity variations between the models were much larger in the inundated land regions. Focusing on the area scale, the V in the inundation leading edge in Region B was smaller than in Region A. Such differences in the inundation leading edge in each region depend on the cross-shore velocity. The major flow direction in Region A was the same as in the offshore (east direction, i.e., $+X$ direction) and the flow direction in Region B was perpendicular to the one in offshore (north direction, i.e., $+Y$ direction). Therefore, the cross-shore velocity at the shoreline was larger in Region A than Region B and it indicated that a larger velocity gave the larger variation.

This tendency might be explained by the differences in advection terms and the wet/dry boundary conditions that considered the effect of the friction term was minor based on the discussion in the previous paragraph. A major source was the difference in the advection term since magnitudes were proportional to the square of the current velocity and this was relatively larger when the current velocity was larger. The wet/dry boundary condition contributed to the variation. The same wet/dry conditions (Kotani et al. 1998) were used in TUNAMI, STOC, and JAGURS but the detailed treatment in the source codes were different in each model although the scheme used was the same. For instance, the application phase of the wet/dry condition was different. TUNAMI and JAGURS applied the wet/dry condition before computation of discharge and STOC did it after computation of velocity in the whole domain.

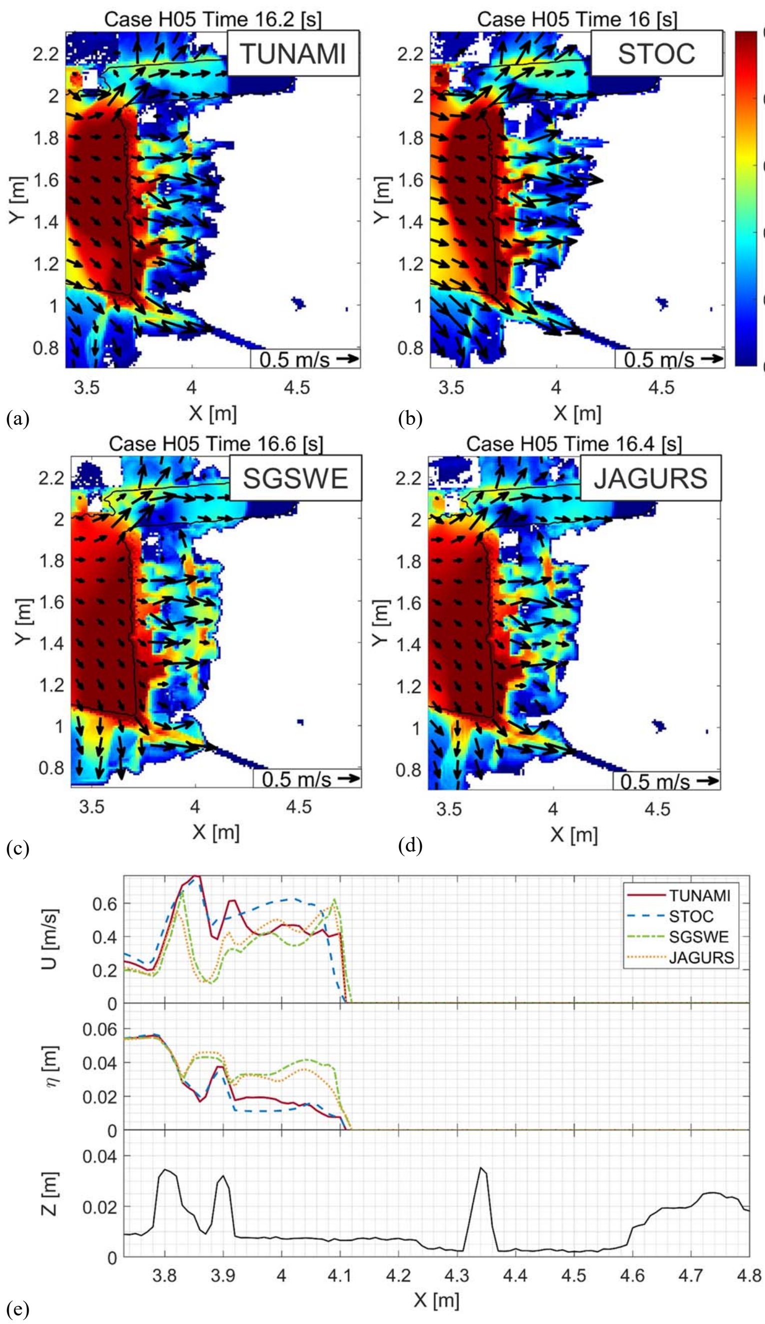

Fig. 11. Model difference of snapshot of inundation process in Region A, when modeled flow, arrives at Buildings Y. (a–d) snapshot of η and current; (a) TUNAMI; (b) STOC; (c) SGSWE; and (d) JAGURS; and (e) cross-sectional change in cross-shore velocity (top), η (middle), and topographic change (bottom) along Profile 1 shown in Fig. 7 (refer Fig. 3).

The effects of tolerance water depth for wet/dry on inundation by the numerical models were small compared with the tsunami scale, because the detailed differences of the wet/dry boundary scheme in their source codes gave a large variation in surface elevation and wavefront velocity. Such differences in surface elevation gave a variation in the current velocity since the current velocity arose from the gradient of surface elevation. Once the velocity variation occurred, the advection term evaluation gave a large variation since the advection term was proportional to the square of the velocity. However, a detailed mechanism was not shown and further investigations that use simpler topography, such as a uniform slope, is needed. Finally, the velocity difference gave the variations in wavefront velocity and arrival time.

In addition, it is important that the arrival time difference gave a further difference in the local inundation process. Region B is a good example to highlight this point. Two flows in the west and south directions merged at the intersection in Region B. The arrival of the flow from the south did not vary due to the small cross-shore velocity explained previously; however, the one from the west was quite different between each model since the cross-shore velocity had the same direction as the main flow. The discrepancy in the merge time created the local difference in surface distribution and current velocity. The earlier arrival time gave a large blocking effect by the flow from the west to the one from the south. in which the large surface elevation around the intersection was calculated as explained in the section "Model Variation and Accuracy of the Spatial Data".

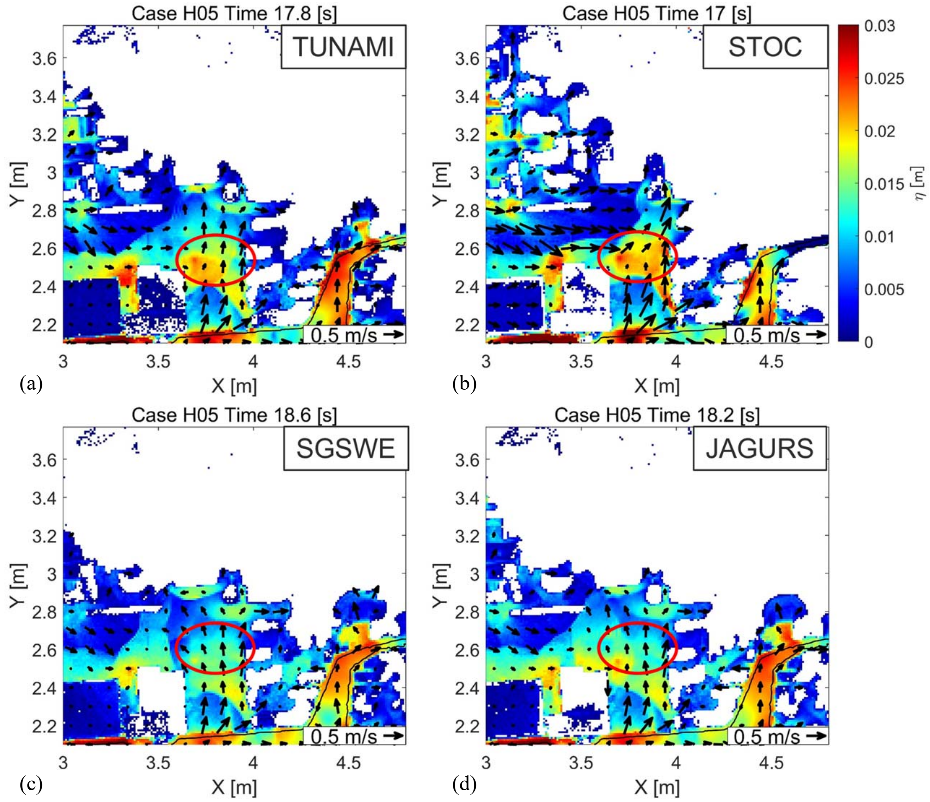

Fig. 12. Model difference of the snapshots of η and current velocity in Region B shown in Fig. 7 when the flows from south and west merge. (a) TUNAMI; (b) STOC; (c) SGSWE; and (d) JAGURS.

Table 2. Summary of calibrated coefficients (λ and ξ) for each empirical fragility (EF) model

Empirical fragility	λ	ξ
EF1	1.58	0.41
EF2	1.73	0.42

Based on the discussions presented in the previous paragraph, the detailed differences in the treatment of the advection term and wet/dry boundary condition gave a variation in the current velocity on the land and the errors between each model accumulated, because the run-up distance was longer due to the iteration process to solve the advection term that used the current velocity in the previous time step. In addition, abrupt topographic changes, such as buildings enlarged the variation in surface elevation and current velocity.

The variations in the maximum inundation depths and fluid velocities that were observed in the inter-model comparison affected the building damage fragility assessment that was calculated from these tsunami intensity factors. The sensitivity analysis for the variations in both intensities is given using fragility models in Hayashi et al. (2013). The fragility model calculated the probability of destruction using either maximum inundation depth or maximum fluid velocity and was developed using linear regression combined with the results of the numerical modeling for the validation of the tsunami front and flow velocities in the 2011 Tohoku Earthquake Tsunami. Refer to the literature for additional information on this topic (e.g., Suppasri et al. 2015; Charvet et al. 2015). The probability of the destruction [$P_D(x)$] is found by

$$P_D(x) = \Phi\left[\frac{\ln x - \lambda}{\xi}\right] \tag{4}$$

where Φ = standardized normal distribution function; x = tsunami intensity measure (e.g., maximum inundation depth or fluid velocity); and λ and ξ = calibrated coefficients for each intensity measure (each value is listed in Table 2). Hayashi et al. assumed that three different structure types were assumed: reinforced concrete (RC), steel, and wooden. Steel was assumed in this comparison since no detailed data about the structures in Kainan, Wakayama, Japan, are available. The functions that used only maximum inundation depth and fluid velocity were denoted as EF1 and EF2, respectively. The tsunami intensity measures at the grid points around the buildings were collected and averaged. Then, $P_D(x)$ for each building that used the collected intensity measures was calculated following Eq. (4). Then, the number of buildings below a specific probability of destruction was calculated. Fig. 13 shows the model variations in the probabilities of building destruction for each different model. EF1 (depth) and EF2 (velocity) showed inter-model fragility variations to some extent. However, EF2 gave larger differences. especially when the probability of destruction was high (>0.6). In addition, EF1 showed a somewhat smaller inter-model variation for each building (V_b), particularly for high probabilities of damage. Note that V_b is calculated by the following formula:

$$V_b = \frac{\sqrt{\frac{1}{N_b}\frac{1}{N_{\text{model}}}\sum_{j=1}^{N_{\text{model}}}\sum_{i=1}^{N_b}(P_{D,i,j} - P_{D,i,\text{mean}})^2}}{P_{D,\text{all-mean}}} \tag{5}$$

where N_{model} (=381) = number of buildings; $N_b (=4)$ = number of SWE models; $P_{D,i,j}$ = probability of the destruction for the ith building estimated by the jth SWE model; and $P_{D,\text{all-mean}}$ = arithmetic average of the probability for all SWE models and buildings. For overall predictions, the EF1 model showed inter-model variation in damage state probability $V_b = 0.16$, compared with $V_b = 0.20$ for the EF2 model. The previous results indicate that

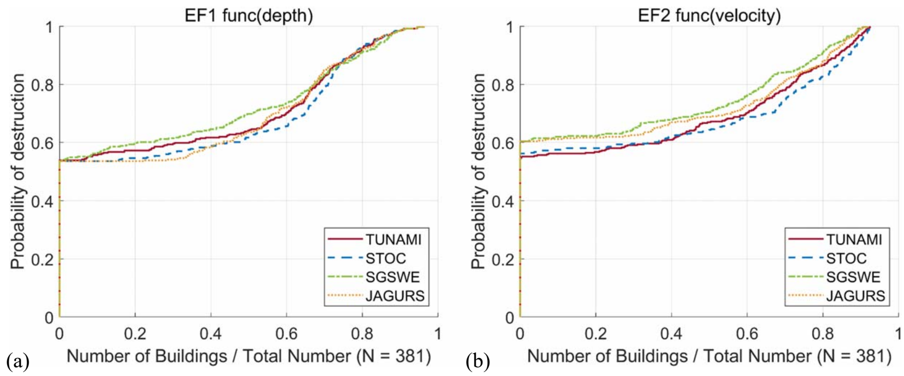

Fig. 13. Predicted probability of building destruction by different models and building ratio out of 381 buildings in total corresponding below a certain probability by two empirical fragility functions: (a) EF1 that used inundation depth; and (b) EF2 that used fluid velocity. Different lines show model differences and corresponds to Fig. 3.

Table 3. Summary of values to calculate dimensionless quantities (*Bo*, *We*, *Re*, and *Fr*)

Symbol	Name	Value
g	Gravitational acceleration	9.81 m/s^2
ρ	Water density	1,000 kg/m^3
ρ_a	Air density	1.29 kg/m^3
$\Delta\rho$	Difference of density	1,000 kg/m^3
L	Characteristic length	0.05 m (average building width in physical model)
U	Characteristic velocity	Average value of maximum velocity in Region A′
γ	Surface tension	0.0728 N/m
ν	Kinematic viscosity	10^{-6} m^2/s

Table 4. Summary of the calculated dimensionless quantities (*Bo*, *We*, *Re*, and *Fr*); upper and lower numbers show values at experimental and full scale, respectively

Symbol	TUNAMI	STOC	SGSWE	JAGURS	Exp
Bo	336.45	336.45	336.45	336.45	336.45
	2.10×10^7	2.10×10^7	2.10×10^7	2.10×10^7	2.10×10^7
We	170.08	275.79	128.29	153.49	198.45
	1.11×10^7	1.72×10^7	0.96×10^7	0.80×10^7	1.24×10^7
Re	22,504	29,264	19,304	21,687	22,992
	8.90×10^7	1.16×10^8	7.63×10^7	8.57×10^7	9.09×10^7
Fr	0.64	0.84	0.55	0.62	0.66
	0.64	0.84	0.55	0.62	0.66

inter-model variation lead to significant differences in the predicted damage and higher sensitivity of the fragility was given by the fluid velocity than the inundation depth.

In addition, the scaling effect that included the surface tension and friction was assessed using the dimensionless quantities, Bond number (*Bo*), Weber number (*We*), Reynolds number (*Re*), and Froude number (*Fr*), which are defined as follows:

$$Bo = \frac{\Delta\rho g L^2}{\gamma} \tag{6}$$

$$We = \frac{\rho U^2 L}{\gamma} \tag{7}$$

$$Re = \frac{UL}{\nu} \tag{8}$$

$$Fr = \frac{U}{\sqrt{gL}} \tag{9}$$

Each variable and its value are summarized in Table 3. The calculated dimensionless quantities in Region A [shown in Fig. 10(a) by a box] are summarized in Table 4. Note that the values of *Fr* did not change between the experimental and full scale since the experiment followed the Froude similitude. *Bo* and *We* related to surface tension were approximately O (10^2), which indicated that the contribution of the surface tension to the gravity and inertial forces might be still small although there was a large difference between the experimental and full scales. The experimental and numerical results showed approximately O (10^4) and O (10^7) for *Re*, respectively. Then, the contribution of the viscosity to the inertial force was still negligible. The drag coefficient for a circular cylinder (C_D) was approximately 1.0 and 0.75 for $Re =$ O (10^4) and O (10^7), respectively (e.g., Roshko 1961). Therefore, the range of resistance force differences from the buildings between the experimental and full scales was within 25%.

In summary, the overall characteristics of the inundation processes, such as the inundation depth, surface elevation, and current velocity could be modeled by the multimodel inundation simulation presented in this study. However, a range in the variation of the detailed inundation process exemplified by merging and blocking and specifically in city areas, such as buildings, bridges, and intersections remained. The uncertainty of the simulated results by the model difference should be considered if a numerical simulation of urban inundation is performed since such inter-model variation in inundation depth or velocity gave significant differences in the building fragility assessment. In addition, the scaling effect that was induced by, for instance, surface tension on the magnitude of surface elevation and fluid velocity could be small for this experimental case although there was a large difference in dimensionless quantities between the experimental and full scale. However, further studies to quantify the scaling effect are recommended.

Conclusions

This study conducted physical and numerical modeling of tsunami inundation in a 3D complex coastal city model that included ports and buildings. The experiments used tsunami conditions for a solitary wave by a piston-type wavemaker, constant flow, and realistic long period tsunami waveforms by a pump. The time series of tsunami wave height was measured by 12 WGs that covered the flume from offshore to onshore and over the city model. The tsunami inundation propagation on the land was recorded by an overhead 4K video camera. Fluorescent dye was used to detect the leading edge of inundation. The PIV was applied to measure the spatial flow pattern and the velocity field were obtained. In addition, this study ran and compared numerical simulations between four different models based on various forms and numerical schemes for the nonlinear shallow water equations. The sensitivity of the tsunami inundation simulations in urban areas was discussed by comparing the simulations with the physical experiment results for the case of solitary wave conditions.

The overall characteristics of inundation, such as the inundation depth, surface elevation, and current velocity could be modeled by the multimodel inundation simulation presented in this study. All the models could reproduce the inundation process overall but the detailed local processes, such as surface elevation at the intersection or the velocity around buildings varied in each model. The variation in the results was confirmed in the detailed inundation process as demonstrated by merging and blocking, specifically in city areas, such as buildings, bridges, and intersections. Fundamental discretization schemes for the bottom friction and advection terms were the same between each model but there were differences in the detailed treatments on their coding. The difference in surface elevation gave the variation in the current velocity since the current velocity was the gradient of surface elevation. Once the velocity variation occurred, the advection term evaluation gave a large variation since the advection term was proportional to the square of the velocity. Considering that the tolerance water depth for the wet/dry boundary was small compared with the tsunami scale, the detailed differences of the wet/dry boundary scheme in their source codes gave a large variation in surface elevation and wavefront velocity. In addition, it is important that the arrival time difference gave a further difference in the local inundation process. The detailed differences in the treatment of the advection term and the wet/dry boundary condition gave a variation in the current velocity on the land and the errors between each model accumulated because the run-up distance was longer due to the iteration process to solve the advection term using the current velocity in the previous time step. Artificial topographic changes, such as buildings enlarged the variation in surface elevation and current velocity. This study confirmed the importance of considering the uncertainty of the modeled results due to model differences in tsunami inundation simulation that target coastal urban areas. The results indicated that inter-model variation lead to significant differences in the predicted damage, and the use of velocities to compute fragility had higher sensitivity to model implementation than using inundation depth.

Data Availability Statement

Some data listed below that support the findings of this study might be available from the corresponding author upon reasonable request. Collected data in the laboratory tests (topography data, water surface at each WG, fluid velocity, and inundation limit).

Acknowledgments

This work was supported by MEXT/JSPS KAKENHI, by JSPS Research Fellow Grant (Fukui, 19J22429), by the Collaborative Research with DPRI, Kyoto University (Yasuda, 2019G-01), the Collaborative Research with DPRI-ERI (Satake, 2019-K-01 and Miyashita, 2021-K-01), JICA/JST SATREPS Mexico Project (Mori), the National Science Foundation under grant 166105 (Kennedy), and by the National Institute of Standards and Technology (Kennedy). The authors are also grateful to Professor T. Hiraishi, Dr. Che-Wei Chang, Mr. M. Kamo (DPRI, Kyoto University), Mr. A. Copp (past undergraduate student at the University of Notre Dame), and Mr. T. Yamamoto (past graduate student in Kansai University) for preparation and conducting of the physical experiment. The authors also acknowledge that anonymous reviewers gave many precious and important comments and suggestions.

Notation

The following symbols are used in this paper:

Bo = Bond number;
Fr = Froude number;
C_D = drag coefficient;
g = gravitational acceleration (m/s^2);
h = water depth of the flume (m);
i = building number;
j = SWE model number;
L = characteristic length (m);
N_b = total number of buildings;
N_{model} = total number of SWE models;
$P_D(x)$ = probability of the destruction;
$P_{D,i,j}$ = $P_D(x)$ for the ith building estimated by the jth SWE model;
$P_{D,i,\mathrm{mean}}$ = arithmetic average of the probability for all SWE models and the ith building;
$P_{D,\mathrm{all\text{-}mean}}$ = arithmetic average of the probability for all SWE models and buildings;
Re = Reynolds number;
T = appearance time of maximum surface elevation time (peak time) (s);
$\bar{T}$ = peak time normalized by the incident wave (s);
T_0 = $\sqrt{h/g}$
U = characteristic velocity (m/s);
V = SWE model dimensionless variation in computed values, such as inundation depth or wave front velocity;
V_b = SWE model dimensionless variation in probability of destruction;
We = Weber number;
x = Tsunami intensity measure (e.g., maximum inundation depth or fluid velocity);
X = horizontal coordinate (m);
Y = vertical coordinate (m);
γ = surface tension (N/m);
η = surface elevation (m);
$\bar{\eta}$ = normalized surface elevation (m);
η_0 = surface elevation at the wave generator (WG1) (m);
λ = calibrated coefficients (one for each intensity measure x);
μ = SWE model mean of computed values;
ν = kinematic viscosity (m^2/s);
ρ = water density (kg/m^3);
ρ_a = air density (kg/m^3);
$\Delta\rho = \rho - \rho_a$ = difference in air and water density (kg/m^3);
ξ = calibrated coefficients (two for each intensity measure x);
σ = SWE model standard deviation of computed values; and
Φ = standardized normal distribution function.

Supplemental Materials

Tables S1, S2 and Fig. S1 are available online in the ASCE Library (www.ascelibrary.org).

References

ASCE. 2016. *Minimum design loads and associated criteria for buildings and other structures*. ASCE/SEI 7-16. Reston, VA: ASCE.

Baba, T., N. Takahashi, Y. Kaneda, K. Ando, D. Matsuoka, and T. Kato. 2015. "Parallel implementation of dispersive tsunami wave modeling with a nesting algorithm for the 2011 Tohoku tsunami." *Pure Appl. Geophys.* 172 (12): 3455–3472. https://doi.org/10.1007/s00024-015-1049-2.

Bagherizadeh, E., Z. X. Zhang, A. Farhadzadeh, D. Angelidis, M. G. Arabi, S. Moghimi, and A. Khosronejad. 2021. "Numerical modelling of solitary wave and structure interactions using level-set and immersed boundary methods by adopting adequate inlet boundary conditions." *J. Hydraul. Res.* 59 (4): 559–585. https://doi.org/10.1080/00221686.2020.1818303.

Casulli, V. 2009. "A high-resolution wetting and drying algorithm for free-surface hydrodynamics." *Int. J. Numer. Methods Fluids* 60 (4): 391–408. https://doi.org/10.1002/fld.1896.

Charvet, I., A. Suppasri, H. Kimura, D. Sugawara, and F. Imamura. 2015. "Fragility estimations for Kesennuma City following the 2011 Great East Japan Tsunami based on maximum flow depths, velocities and debris impact, with evaluation of the ordinal model's predictive accuracy." *Nat. Hazard.* 79 (3): 2073–2099. https://doi.org/10.1007/s11069-015-1947-8.

Chow, V. T. 1959. *Open-channel hydraulics*. New York: McGraw-Hill.

Cox, D. T., T. Tomita, P. Lynett, and R. Holman. 2008. "Tsunami inundation with macro-roughness in the constructed environment." In *Proc., 31st Int. Conf. on Coastal Eng.*, 1421–1432. Reston, VA: ASCE.

Goto, C., Y. Ogawa, N. Shuto, and F. Imamura. 1997. *Numerical method of tsunami simulation 644 with the leap-frog scheme (IUGG/IOC time project)*. IOC Manual, Rep. No. 35. London: UNESCO.

Hayashi, S., Y. Narita, and S. Koshimura. 2013. "Developing tsunami fragility curves from the surveyed data and numerical modeling of the 2011 Tohoku earthquake tsunami." [In Japanese.] *J. Jpn. Soc. Civ. Eng. Coast. Eng.* 69 (2): I_386–I_390. https://doi.org/10.2208/kaigan.69.I_386.

Hiraishi, T., T. Yasuda, N. Mori, R. Azuma, H. Mase, A. Prasetyo, and S. Okura. 2015. "Characteristics of tsunami generator newly implemented with three generation modes." [In Japanese.] *J. Jpn. Soc. Civ. Eng. Coast. Eng.* 71 (2): I_349–I_354. https://doi.org/10.2208/kaigan.71.I_349.

Kennedy, A. B., D. Wirasaet, A. Begmohammadi, T. Sherman, D. Bolster, and J. C. Dietrich. 2019. "Subgrid theory for storm surge modeling." *Ocean Model.* 144: 101491. https://doi.org/10.1016/j.ocemod.2019.101491.

Kotani, M., F. Imamura, and N. Shuto. 1998. "Tsunami run-up simulation and damage estimation by using GIS." [In Japanese.] *Proc. Coast. Eng., JSCE* 45: 356–360. https://doi.org/10.2208/proce1989.45.356.

Le, T. A., H. Takagi, M. Heidarzadeh, Y. Takata, and A. Takahashi. 2019. "Field surveys and numerical simulation of the 2018 Typhoon Jebi: Impact of high waves and storm surge in semi-enclosed Osaka Bay, Japan." *Pure Appl. Geophys.* 176 (10): 4139–4160. https://doi.org/10.1007/s00024-019-02295-0.

Lynett, P. 2016. "Precise prediction of coastal and overland flow dynamics: A grand challenge or a fool's errand." *J. Disaster Res.* 11 (4): 615–623. https://doi.org/10.20965/jdr.2016.p0615.

Lynett, P. J., et al. 2017. "Inter-model analysis of tsunami-induced coastal currents." *Ocean Model.* 114: 14–32. https://doi.org/10.1016/j.ocemod.2017.04.003.

Mizobata, Y., T. Yasuda, Y. Okumura, N. Mori, H. Mase, and H. Shimada. 2014. "Resistance capacity assessment of local communities against tsunami inundations by continuous increase in tsunami intensity." [In Japanese.] *J. Jpn. Soc. Civ. Eng. Coast. Eng.* 70 (2): I_1326–I_1330.

Mori, N., D. T. Cox, T. Yasuda, and H. Mase. 2013. "Overview of the 2011 Tohoku Earthquake Tsunami damage and its relation to coastal protection along the Sanriku coast." *Earthquake Spectra* 29 (S1): 127–143. https://doi.org/10.1193/1.4000118.

Mori, N., T. Takahashi, T. Yasuda, and H. Yanagisawa. 2011. "Survey of 2011 Tohoku Earthquake Tsunami inundation and run-up." *Geophys. Res. Lett.* 38 (7): L049210. https://doi.org/10.1029/2011GL049210.

Park, H., D. Cox, P. J. Lynett, D. M. Wiebe, and S. Shin. 2013. "Tsunami inundation modeling in constructed environments: A physical and numerical comparison of free-surface elevation, velocity, and momentum flux." *Coastal Eng.* 79: 9–21. https://doi.org/10.1016/j.coastaleng.2013.04.002.

Prasetyo, A., T. Yasuda, T. Miyashita, and N. Mori. 2019. "Physical modeling and numerical analysis of tsunami inundation in a coastal city." *Front. Built. Environ.* 5: 46. https://doi.org/10.3389/fbuil.2019.00046.

Pringgana, G., L. S. Cunningham, and B. D. Rogers. 2021. "Influence of orientation and arrangement of structures on tsunami impact forces: Numerical investigation with smoothed particle hydrodynamics." *J. Waterway, Port, Coastal, Ocean Eng.* 147 (3): 04021006. https://doi.org/10.1061/(ASCE)WW.1943-5460.0000629.

Qin, X., M. Motley, R. LeVeque, F. Gonzalez, and K. Mueller. 2018a. "A comparison of a two-dimensional depth-averaged flow model and a three-dimensional RANS model for predicting tsunami inundation and fluid forces." *Nat. Hazards Earth Syst. Sci.* 18 (9): 2489–2506. https://doi.org/10.5194/nhess-18-2489-2018.

Qin, X., M. R. Motley, and N. A. Marafi. 2018b. "Three-dimensional modeling of tsunami forces on coastal communities." *Coastal Eng.* 140: 43–59. https://doi.org/10.1016/j.coastaleng.2018.06.008.

Roshko, A. 1961. "Experiments on the flow past a circular cylinder at very high Reynolds number." *J. Fluid Mech.* 10 (3): 345–356. https://doi.org/10.1017/S0022112061000950.

Sarjamee, S., I. Nistor, and A. Mohammadian. 2017. "Large eddy simulation of extreme hydrodynamic forces on structures with mitigation walls using OpenFOAM." *Nat. Hazard.* 85 (3): 1689–1707. https://doi.org/10.1007/s11069-016-2658-5.

Sogut, E., D. V. Sogut, and A. Farhadzadeh. 2019. "Effects of building arrangement on flow and pressure fields generated by a solitary wave interacting with developed coasts." *Adv. Water Resour.* 134: 103450. https://doi.org/10.1016/j.advwatres.2019.103450.

Sogut, E., D. V. Sogut, and A. Farhadzadeh. 2020. "Overland wave propagation and load distribution among arrays of elevated beachfront structures." *J. Waterway, Port, Coastal Ocean Eng.* 146 (4): 04020016. https://doi.org/10.1061/(ASCE)WW.1943-5460.0000579.

Suppasri, A., I. Charvet, K. Imai, and F. Imamura. 2015. "Fragility curves based on data from the 2011 Tohoku-Oki tsunami in Ishinomaki city, with discussion of parameters influencing building damage." *Earthquake Spectra* 31 (2): 841–868. https://doi.org/10.1193/053013EQS138M.

Tomiczek, T., A. Prasetyo, N. Mori, T. Yasuda, and A. Kennedy. 2016. "Physical modelling of tsunami onshore propagation, peak pressures, and shielding effects in an urban building array." *Coastal Eng.* 117: 97–112. https://doi.org/10.1016/j.coastaleng.2016.07.003.

Tomita, T., and T. Kakinuma. 2005. "Storm surge and tsunami simulation in oceans and coastal areas (STOC)." [In Japanese.] *Rep. Port Airport Res. Inst.* 44 (2): 83–98.

Wang, H., A. Mostafizi, L. A. Cramer, D. Cox, and H. Park. 2016. "An agent-based model of a multimodal near-field tsunami evacuation: Decision-making and life safety." *Transp. Res. Part C Emerging Technol.* 64: 86–100. https://doi.org/10.1016/j.trc.2015.11.01.

Yasuda, T., T. Miyaue, A. Prasetyo, M. Kamo, N. Mori, and T. Hiraishi. 2016. "Tsunami inundation experiment using coastal city model." [In Japanese.] *J. Jpn. Soc. Civ. Eng. Coast. Eng.* 72 (2): I_385–I_390. https://doi.org/10.2208/kaigan.72.I_385.